INTERNATIONAL JOURNAL FOR NUMERICAL AND ANALYTICAL METHODS IN GEOMECHANICS
*Int. J. Numer. Anal. Meth. Geomech.* 2012; **36**:1194–1219
Published online 22 June 2011 in Wiley Online Library (wileyonlinelibrary.com). DOI: 10.1002/nag.1046

# Viscoelastic functionally graded finite element method with recursive time integration and applications to flexible pavements

Eshan V. Dave[1,*,†,‡], Glaucio H. Paulino[2,§] and William G. Buttlar[2,¶,‖]

[1]*Department of Civil Engineering, University of Minnesota Duluth, 254 SCiv, 1405 University Drive, Duluth, MN 55812, U.S.A.*
[2]*Department of Civil and Environmental Engineering, University of Illinois at Urbana—Champaign, 205 N. Mathews Avenue, Urbana, IL 61801, U.S.A.*

SUMMARY

The finite-element (FE) method is used for modeling geotechnical and pavement structures exhibiting significant non-homogeneity. Property gradients generated due to non-homogeneous distributions of moisture is one such example for geotechnical materials. Aging and temperature-induced property gradients are common sources of non-homogeneity for asphalt pavements. Investigation of time-dependent behavior combined with functionally graded property gradation can be accomplished by means of the non-homogeneous viscoelastic analysis procedure. This paper describes the development of a generalized isoparametric FE formulation to capture property gradients within elements, and a recursive formulation for solution of hereditary integral equations. The formulation is verified by comparison with analytical and numerical solutions. Two application examples are presented: the first describes stationary crack-tip fields for viscoelastic functionally graded materials, and the second example demonstrates the application of the proposed procedures for efficient and accurate simulations of interfaces between layers of flexible pavement. Copyright © 2011 John Wiley & Sons, Ltd.

Received 2 September 2009; Revised 16 December 2010; Accepted 8 March 2011

KEY WORDS: flexible pavements; generalized isoparametric formulation (GIF); viscoelasticity; viscoelastic functionally graded materials (VFGM); hereditary integrals

## 1. INTRODUCTION

As of October 2008, there are over 2.6-million miles of paved roads across the United States, out of which 75.6% have an asphalt concrete surface [1]. Asphalt concrete pavements are inherently graded viscoelastic structures. Oxidative aging of asphalt binder and temperature cycling leading to gradients in temperature with depth are the major cause of non-homogeneity. Current pavement analysis and simulation procedures predominantly use a layered approach to account for these non-homogeneities; a common example of such approach is the recently developed American Association of State Highway and Transportation Officials (AASHTO) Mechanistic-Empirical Design Guide (MEPDG) [2].

*Correspondence to: Eshan V. Dave, Department of Civil Engineering, University of Minnesota Duluth, 254 SCiv, 1405 University Drive, Duluth, MN 55812, U.S.A.
†E-mail: evdave@umn.edu
‡Assistant Professor.
§Donald Biggar Willet Professor of Engineering.
¶Professor.
‖Narbey Khachaturian Faculty Scholar.

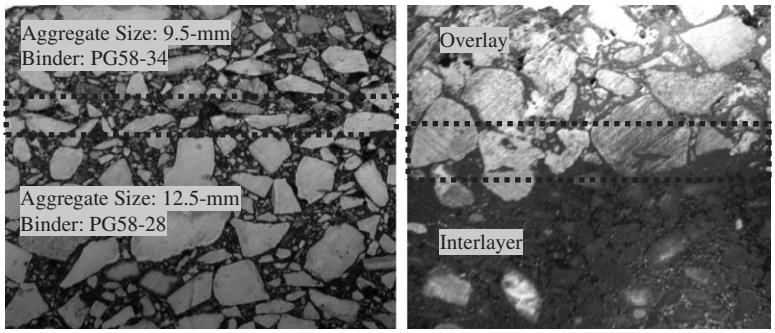


Figure 1. Cross-section of asphalt pavements showing interfacial zone between different construction courses.

It is a common practice to design and construct asphalt concrete pavement layers in a number of different courses ranging from 18 mm ($\frac{3}{4}$ in) to 75 mm (3 in) in thickness. The interfaces between these layers form a continuously graded zone of finite thickness. For pavements designed and constructed with layers of significantly different properties, it is critical to give attention to the graded nature of the interface. Typical examples of pavement systems with significantly different materials include overlay–interlayer systems, surface treatments with open-graded mixtures laid on top of dense-graded mixtures, and special treatments that yield varying asphalt binder content through the thickness of course such as chip seals or bonded overlays. The interfaces of different construction lifts are shown in Figure 1 for two asphalt pavements. The boxes (dotted lines) indicate the region of the interface where rapid transitioning between the two distinct layers occurs. Unless this transition zone is properly accounted for in analysis, significant numerical artifacts may occur, such as unrealistically high shear stress at the interface.

Functionally graded materials (FGMs) are characterized by spatially varied microstructures created by non-uniform distributions of the reinforcement phase with different properties, sizes, and shapes, as well as by interchanging the role of reinforcement and matrix materials in a continuous manner [3]. They are usually engineered to produce property gradients aimed at optimizing structural response under different types of loading conditions (thermal, mechanical, electrical, optical, etc.) [4]. These property gradients are produced in several ways, for example by gradual variation of the content of one phase relative to other, or by using a sufficiently large number of constituent phases with different properties [5].

Flexible pavements are one of several civil engineering systems exhibiting viscoelastic functionally graded material (VFGM) behavior. Many geotechnical materials exhibit viscoelastic characteristics, for example, behavior of sands as recently demonstrated by Bang *et al.* [6]. Factors such as moisture distribution [7, 8], temperature non-homogeneity [9], pore distribution [10], etc. commonly yield functionally graded viscoelastic boundary value problems in geotechnical engineering. Other examples of such systems include graded fiber- reinforced cement and concrete structures [11]. Application areas for the graded viscoelastic analysis include accurate simulation of the interfaces between viscoelastic materials such as the layer interface between different asphalt concrete lifts.

The homogeneous finite-element modeling (FEM) technique discretizes the problem domain into smaller elements, each with a unique constitutive property. The capability to effectively discretize the problem domain makes it an attractive simulation technique. However, the assignment of a single material property description to an element in the FEM approach makes it an unattractive choice for simulation of problems with material non-homogeneities. Specialized elements, such as 'graded elements', allow for non-homogenous material property definitions within an element. This paper describes the development and verification of the graded viscoelastic finite-element (FE) analysis method and some of its applications.

This paper is organized into six subsequent sections. The background and related research work is described followed by the introduction of the basic viscoelastic FE framework. A recursive



DOI: 10.1002/nag

time-integration scheme is introduced next, which is followed by a series of verifications through comparisons with analytical and numerical solutions. The later portion of this paper describes two application examples: the first one describing crack-tip stress fields for VFGM and the second one presents responses of flexible pavement systems with graded interfaces. Finally, conclusions and future extensions of the present work are presented.

## 2. BACKGROUND AND RELATED WORK

Analytical solutions have been developed for a variety of functionally graded viscoelastic problems such as fracture [12, 13] and plate bending [14]. For analysis of complex boundary value problems, such as flexible pavements or geotechnical structures, numerical analysis procedures are preferred due to lack of analytical solutions. For example, the latest pavement design guide developed by AASHTO [15] relies on FE analysis for the evaluation of stress and strain responses under tire loading.

Specialized 'graded elements' have been previously proposed for simulation of FGMs, among others by Santare and Lambros [16], and Kim and Paulino [17]. Two common approaches have been proposed: (1) direct Gaussian integration and (2) the generalized isoparametric formulation (GIF). The GIF relies on natural extension of the conventional iso-parametric mapping to capture material non-homogeneity within the element. The GIF has been explored for variety of elastic FGM problems such as dynamic behavior of beams [18]. Recently, Silva *et al.* [19] showed the benefits and suitability of using GIF for multiphysics applications.

Extensive research has been conducted in the area of numerical analysis of viscoelastic problems. The literature can be divided into two categories: (1) transformation-based or correspondence principle-based methods and (2) time-integration methods. Examples of these approaches include works by Hilton and Yi [20], which describe a transformation-based approach for anisotropic viscoelastic composites, and a recursive time-integration scheme for orthotropic and non-linear viscoelastic problems as described by Muliana and Khan [21]. A variety of time-integration schemes have been explored for viscoelastic FEs such as incremental schemes [22, 23] and recursive schemes [21, 24, 25]. Incremental schemes are based on the determination of response increment in each time-step, whereas recursive schemes rely on keeping track of the material history effect and updating it at each time-step.

A limited amount of work has been conducted on numerical simulation of viscoelastic FGMs including meshless and boundary integrals methods [26, 27] and correspondence principle-based FEs [28]. These previous approaches rely on the use of integral transformations and therefore they are imposed with the limitations of the correspondence principle as described by Mukherjee and Paulino [29] and Rajagopal and Wineman [30]. The time-integration approaches are not imposed with limitations on material model description or boundary conditions as required by the correspondence principle; hence in this study, the time-integration approach is explored. Details of the recursive time-integration scheme in conjunction with viscoelastic GIF for FEs are described later in this paper.

## 3. BASIC VISCOELASTIC FE FORMULATION

The basic stress–strain relationships for viscoelastic materials have been presented by, among others, Hilton [31] and Christensen [32]. The constitutive relationship for a quasi-static, linear viscoelastic isotropic materials is given as

$$\sigma_{ij}(x_i,t) = 2\int_{t'=-\infty}^{t'=t} G(x_i,\xi(t)-\xi(t'))\left(\varepsilon_{ij}(x_i,t')-\frac{1}{3}\delta_{ij}\varepsilon_{kk}\right)\mathrm{d}t' + \int_{t'=-\infty}^{t'=t} K(x_i,\xi(t)-\xi(t'))\delta_{ij}\varepsilon_{kk}\,\mathrm{d}t' \quad (1)$$



DOI: 10.1002/nag

where $\sigma_{ij}$ are stresses and $\varepsilon_{ij}$ are strains at any location $x_i$. The parameters $G$ and $K$ are the shear and bulk relaxation moduli, respectively, $\delta_{ij}$ is the Kronecker delta, and $t'$ is the integration variable. Subscripts $(i, j, k, l = 1, 2, 3)$ follow Einstein's summation convention. The reduced time $\xi$ is related to real time $t$ and temperature $T$ through the time–temperature superposition principle:

$$\xi(t) = \int_0^t a(T(t'))\,\mathrm{d}t' \tag{2}$$

For a non-homogeneous viscoelastic body in a quasi-static condition, assuming a boundary value problem with displacement $u_i$ on volume $\Omega_u$, traction $P_i$ on surface $\Omega_\sigma$, and body force $F_i$, the equilibrium and strain–displacement relationships (for small deformations) are as shown in Equation (3),

$$\sigma_{ij,j} + F_i = 0, \quad \varepsilon_{ij} = \tfrac{1}{2}(u_{i,j} + u_{j,i}) \tag{3}$$

respectively, where $u_i$ is displacement and $(\cdot)_{,j} = \partial(\cdot)/\partial x_j$.

The derivation of FE formulations using variational principles is described by many authors, including the textbooks by Cook *et al.* [33] and Reddy [34]. The variational principle for quasi-static linear viscoelastic materials under isothermal conditions can be found in Gurtin [35]. Taylor *et al.* [23] extended it for thermo-viscoelastic boundary value problems,

$$\begin{aligned}\pi = &\int_{\Omega_u}\int_{t'=-\infty}^{t'=t}\int_{t''=-\infty}^{t''=t-t'} \frac{1}{2} C_{ijkl}[x_i, \xi_{ijkl}(t-t'') - \xi'_{ijkl}(t')] \frac{\partial \varepsilon_{ij}(x_i, t')}{\partial t'} \frac{\partial \varepsilon_{kl}(x_i, t'')}{\partial t''}\,\mathrm{d}t'\,\mathrm{d}t''\,\mathrm{d}\Omega_u \\ &- \int_{\Omega_u}\int_{t'=-\infty}^{t'=t}\int_{t''=-\infty}^{t''=t-t'} C_{ijkl}[x_i, \xi_{ijkl}(t-t'') - \xi'_{ijkl}(t')] \frac{\partial \varepsilon^*_{ij}(x_i, t')}{\partial t'} \frac{\partial \varepsilon^*_{kl}(x_i, t'')}{\partial t''}\,\mathrm{d}t'\,\mathrm{d}t''\,\mathrm{d}\Omega_u \\ &- \int_{\Omega_\sigma}\int_{t''=-\infty}^{t''=t} P_i(x_i, t-t'') \frac{\partial u_i(x_i, t'')}{\partial t''}\,\mathrm{d}t''\,\mathrm{d}\Omega_\sigma \end{aligned} \tag{4}$$

where $\pi$ is the potential for the body, $\Omega_u$ is the volume, $\Omega_\sigma$ is the surface on which tractions $P_i$ are prescribed, $u_i$ are the displacements, $C_{ijkl}$ are space- and time-dependent material constitutive properties, $\varepsilon_{ij}$ are the mechanical strains and $\varepsilon^*_{ij}$ are the thermal strains, and $\xi_{ijkl}$ is the reduced time related to real time, $t$, and temperature, $T$, through time-temperature superposition principle of Equation (2). The first variation provides the basis for the FE formulation

$$\begin{aligned}\delta\pi = &\int_{\Omega_u}\int_{t'=-\infty}^{t'=t}\int_{t''=-\infty}^{t''=t-t'} \left\{ \begin{array}{l} C_{ijkl}[x_i, \xi_{ijkl}(t-t'') - \xi'_{ijkl}(t')] \\ \dfrac{\partial}{\partial t'}(\varepsilon_{ij}(x_i, t') - \varepsilon^*_{ij}(x_i, t')) \dfrac{\partial \delta\varepsilon_{kl}(x_i, t'')}{\partial t''} \end{array} \right\} \mathrm{d}t'\,\mathrm{d}t''\,\mathrm{d}\Omega_u \\ &- \int_{\Omega_\sigma}\int_{t''=-\infty}^{t''=t} P_i(x_i, t-t'') \frac{\partial \delta u_i(x_i, t'')}{\partial t''}\,\mathrm{d}t''\,\mathrm{d}\Omega_\sigma = 0 \end{aligned} \tag{5}$$

The element displacement vector, $u_i^{\mathrm{el}}$, is related to nodal displacement degrees of freedom (dof) $q$ through the shape functions, $N_{ij}$,

$$u_i^{\mathrm{el}}(x_i, t) = N_{ij}(x_i) q_j(t) \tag{6}$$

Differentiation of Equation (6) yields the relationship among strain, $\varepsilon_i$, nodal displacements, $q_i$, and derivatives of shape functions, $B_{ij}$,

$$\varepsilon_i(x_i, t) = B_{ij}(x_i) q_j(t) \tag{7}$$

Equations (5)–(7) provide the equilibrium equation for each FE,

$$\int_0^t k_{ij}(x_i, \xi(t) - \xi(t')) \frac{\partial q_j(t')}{\partial t'}\,\mathrm{d}t' = f_i(x_i, t) + f_i^{\mathrm{th}}(x_i, t) \tag{8}$$



DOI: 10.1002/nag

where $k_{ij}$ is the element stiffness matrix, $f_i$ is the mechanical force vector, and $f_i^{\text{th}}$ is the thermal force vector, which are described as follows:

$$k_{ij}(x_i,t)=\int_{\Omega_u} B_{ik}^T(x_i)C_{klmn}(x_k,\xi(t))B_{nj}(x_n)\,\mathrm{d}\Omega_u \tag{9}$$

$$f_i(x_i,t)=\int_{\Omega_\sigma} N_{ij}(x_i)P_j(x_j,t)\,\mathrm{d}\Omega_\sigma \tag{10}$$

$$f_i^{\text{th}}(x_i,t)=\int_{\Omega_u}\int_{-\infty}^{t} B_{ik}(x_i)C_{klmn}(x_k,\xi(t)-\xi(t'))\frac{\partial\varepsilon_n^*(x_n,t')}{\partial t'}\,\mathrm{d}t'\,\mathrm{d}\Omega_u \tag{11}$$

$$\varepsilon_n^*(x_n,t)=\alpha(x_n)\Delta_T(x_n,t) \tag{12}$$

where $\alpha$ is the coefficient of thermal expansion and $\Delta_T$ is the temperature change with respect to initial conditions.

On assembly of the individual FE contributions for the given problem domain, the global equilibrium equation can be obtained as

$$\int_0^t K_{ij}(x_i,\xi(t)-\xi(t'))\frac{\partial u_j(t')}{\partial t'}\,\mathrm{d}t'=F_i(x_i,t)+F_i^{\text{th}}(x_i,t) \tag{13}$$

where $K_{ij}$ is the global stiffness matrix, $u_i$ is the global displacement vector and $F_i$ and $F_i^{\text{th}}$ are the global mechanical and thermal force vectors, respectively. The solution to the problem requires solving the convolution shown above to determine nodal displacements.

In previous analysis using the FE method, a single set of properties were assigned to each element [36–38]. In the case of graded elements with GIF, the constitutive material properties are selected at each node point and interpolated back to the Gauss-quadrature points (Gaussian integration points) using isoparametric shape functions. Using GIF, the non-homogeneous viscoelastic material properties such as shear relaxation modulus $G(t)$ and bulk relaxation modulus $K(t)$ are interpolated as

$$G(t)=\sum_{i=1}^{m} N_i[G(t)]_i,\quad K(t)=\sum_{i=1}^{m} N_i[K(t)]_i \tag{14}$$

where $N_i$ are the iso-parametric shape functions corresponding to node $i$, and $m$ is the number of nodal points in the element.

## 4. RECURSIVE TIME-INTEGRATION FORMULATION

The recursive integration scheme based on the formulation by Yi and Hilton [25] is presented in this section for viscoelastic FGM elements. Comparisons between the direct integration and recursive approaches for homogeneous and FGM viscoelastic problems are made and the results are described later in this section. The subsequent sections describe more rigorous verification and validation examples.

For a viscoelastic FGM represented by a generalized Maxwell model with $h$ units, the kernel $K_{ij}$ expands as

$$K_{ij}(x_i,\xi)=\sum_{h=1}^{m}(K_{ij}^e(x_i))_h\,\mathrm{Exp}\left(-\frac{\xi(t)}{(\tau_{ij}(x_i))_h}\right) \tag{15}$$

A simplified representation of the generalized Maxwell model utilized in the above equation is shown in Figure 2. The relaxation times for $h^{\text{th}}$ Maxwell unit is $(\tau_{ij})_h$, which is given in terms of the ratio of viscous parameters $(\eta_{ij})_h$ and elastic parameters $(K_{ij}^e)_h$.



DOI: 10.1002/nag

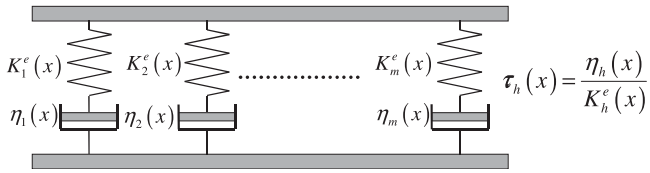


Figure 2. Generalized Maxwell model.

The nodal displacements, $u_j$, and its time derivatives, $\dot{u}_j$ and $\ddot{u}_j$, can be approximated as

$$\begin{aligned} u_j(t_n) &= u_j(t_{n-1}) + \frac{\partial u_j(t)}{\partial t}\Delta t + \frac{\partial^2 u_j(t)}{\partial t^2}\left(\frac{\Delta t}{2}\right)^2, \quad t_{n-1} \leqslant t \leqslant t_n \\ \frac{\partial u_j(t)}{\partial t} &= \dot{u}_j(t_n) = \frac{u_j(t_n) - u_j(t_{n-1})}{\Delta t} \\ \frac{\partial^2 u_j(t)}{\partial t^2} &= \ddot{u}_j(t_n) = \frac{\dot{u}_j(t_n) - \dot{u}_j(t_{n-1})}{\Delta t} \end{aligned} \tag{16}$$

where $t_n$ is the time at increment $n$ and $\Delta t$ is the time-step size.

Using assumptions shown in Equation (16), the kernel form in Equation (15), and by performing integration by parts, the viscoelastic FGM FE problem described in Equation (13) can be expressed as

$$\begin{aligned} &\left[\sum_{h=1}^{m}(K_{ij}^e(x_i))_h \cdot [(v_{ij}^1(x_i,t_n))_h \Delta t - (v_{ij}^2(x_i,t_n))_h]\frac{2}{\Delta t^2}\right] u_j(t_n) \\ &= F_i(t_n) + \sum_{h=1}^{m}\left[\left[(K_{ij}^e(x_i))_h \cdot \mathrm{Exp}\left[-\frac{\xi(t_n)}{(\tau_{ij}(x_i))_h}\right]\right]\left\{(v_{ij}^1(x_i,t_{n-1}))_h\left[u_j(t_{n-1})\frac{2}{\Delta t} + \dot{u}_j(t_{n-1})\right]\right.\right. \\ &\left.\left. -\frac{2}{\Delta t^2}(v_{ij}^2(x_i,t_{n-1}))_h[u_j(t_{n-1}) + \dot{u}_j(t_{n-1})\Delta t] - u_i(t_0) + (v_{ij}^1(x_i,t_0))\dot{u}_j(t_0)\right\} + (R_i(t_n))_h\right] \end{aligned} \tag{17}$$

where the viscous terms in the current time-step $v_{ij}^1$ and $v_{ij}^2$, and the recursive term $R_i$ are given as

$$\begin{aligned} (v_{ij}^1(x_i,t_n))_h &= \int_0^{t_n} \mathrm{Exp}[-\xi(t')/(\tau_{ij}(x_i))_h]\,\mathrm{d}t' \\ (v_{ij}^2(x_i,t_n))_h &= \int_{t_{n-1}}^{t_n} (v_{ij}^1(x_i,t'))_h\,\mathrm{d}t' \\ (R_i(t_n))_h &= K_{ij}^e \cdot \mathrm{Exp}[-\xi(t')/(\tau_{ij}(x_i))_h] \cdot (v_{ij}^2(x_i,t_n))_h \ddot{u}_j(t_{n-1}) \\ &\quad + \mathrm{Exp}[-\xi(t')/(\tau_{ij}(x_i))_h](R_j(t_{n-1}))_h \end{aligned} \tag{18}$$

Notice that in the above expression, the solution at any time, $t_n$, is dependent on the second derivative of displacements, $\ddot{u}_j(t_{n-1})$, and the recursive term, $R_j(t_{n-1})$, from the previous time-step. This property of the recursive schemes makes it computationally efficient when compared with the direct integration approaches that require access and use of solutions from all the previous time-steps.

FE implementation has been performed for solving two-dimensional (2D) planar and axisymmetric problems. Implementation is done to conduct simulations using software Matlab. At present linear interpolation (shape) functions are implemented. A viscoelastic boundary value problem



DOI: 10.1002/nag

Table I. Computation times for different solution schemes (creep problem).

| | Solution time (ms) | | |
|---|---|---|---|
| Step size (s) | Direct integration | Recursive formulation (relative reduction in solution time compared direct integration is shown in parenthesis) | Correspondence principle-based analysis [28] |
| 0.01 | 1.6E+06 | 8.6E+05 (46.5%) | 1.1E+06 |
| 0.02 | 8.6E+05 | 4.5E+05 (47.7%) | |
| 0.05 | 3.9E+05 | 2.1E+05 (46.2%) | |
| 0.1 | 2.0E+05 | 9.7E+04 (51.5%) | |
| 0.2 | 8.2E+04 | 4.7E+04 (42.7%) | |
| 0.5 | 4.3E+04 | 1.6E+04 (62.8%) | |
| 1 | 1.8E+04 | — | |

Table II. Error analysis for different solution schemes (creep problem).

| | Cumulative absolute error | | |
|---|---|---|---|
| Step size (s) | Direct integration | Recursive formulation (ratio of the cumulative absolute error between recursive formulation and direct integration are shown in parenthesis) | Correspondence principle-based analysis [28] |
| 0.01 | 0.005 | 0.0143 (2.86) | 0.162 |
| 0.02 | 0.011 | 0.0319 (2.90) | |
| 0.05 | 0.027 | 0.0675 (2.50) | |
| 0.1 | 0.059 | 0.1558 (2.64) | |
| 0.2 | 0.108 | 0.3746 (3.47) | |
| 0.5 | 0.269 | 0.9039 (3.36) | |
| 1 | 1.026 | — | |

simulating 100 s creep extension of a bar is simulated using recursive and direct integration methods. The computational times and solution accuracy are determined for different time-step sizes.

The same boundary value problem was solved using the correspondence principle-based formulation described by Dave *et al.* [28]. The computational times and error analysis for different time-step sizes are tabulated in Tables I and II. Notice that cumulative errors over the analysis period are tabulated. The analysis results are as expected, with larger computational times and lower errors for smaller time-steps. The general observation from this example shows greater computational cost for direct integration compared with recursive formulation; this is due to continuous access and computations utilizing all the previous solutions at each increment. The solution accuracy for both time-integration approaches depend on the time-step sizes. Recursive formulation requires smaller time-steps compared with direct integration for the same level of accuracy. The problem shown here is quite simple as far as problem geometry, size, and boundary conditions are concerned. The computational efficiency benefits of the recursive scheme are expected to be better for larger problems with complicated boundary conditions. In order to demonstrate this and to present a more convincing case for use of recursive scheme over direct integration, an example of a viscoelastic body with cyclic loading is presented next.

### *4.1. Viscoelastic body with cyclic loading*

A viscoelastic body is simulated with sinusoidal loading conditions. The load is applied at a frequency of 0.5 Hz. The problem geometry, boundary conditions, and FE mesh are shown in Figure 3. The viscoelastic material properties are shown in Figure 4. The properties are simulated with generalized Maxwell model consisting of five Maxwell units. The exact (analytical) solution to this problem can be evaluated and is available in standard references in viscoelasticity, such as



DOI: 10.1002/nag

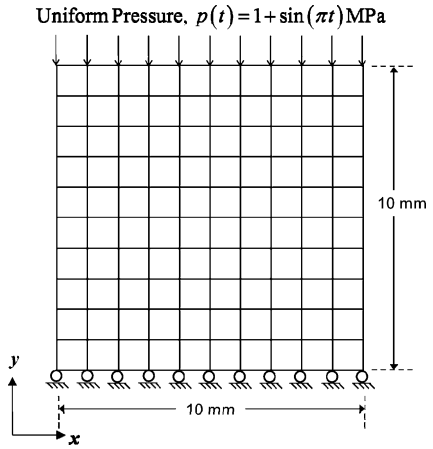


Figure 3. Problem description for example with sinusoidal loading (problem geometry, boundary conditions, and finite element mesh).

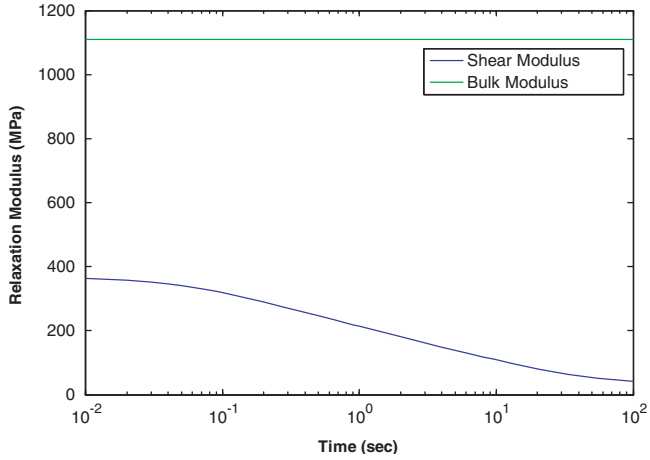


Figure 4. Relaxation modulus for example with sinusoidal loading.

Christensen [32]. The response of viscoelastic bodies imposed with cyclic pressure loading can be expressed in terms of two important parameters, the phase lag between imposed stress and the corresponding strain, and the total strain accumulation at any given time of loading. For the example presented here, the imposed stress and the corresponding strain response are shown in Figure 5.

The problem was solved using direct integration and recursive integration scheme with various time increment sizes ranging from 0.001 to 0.2 s. The results from each set of simulations were compared against the analytical solution. The strain phase lag and total strain at 100 s were used for making comparisons. The computation times were also evaluated for each run. The absolute deviations from the analytical solution as well as computation times are presented in Table III. Close inspection of the absolute error and computation times from both methods indicate that for similar level of accuracy, the recursive scheme is notably efficient. For example, the errors are similar for direct integration with 0.02 s time-step size and recursive scheme with 0.01 s step size. With these time-step sizes for each method, the recursive scheme is approximately 79% faster. Once again notice that this problem only consists of single cyclic loading with relatively small problem (242 dof); as problems become larger, such as flexible pavements, the benefits of using the recursive method will continue to improve.



DOI: 10.1002/nag

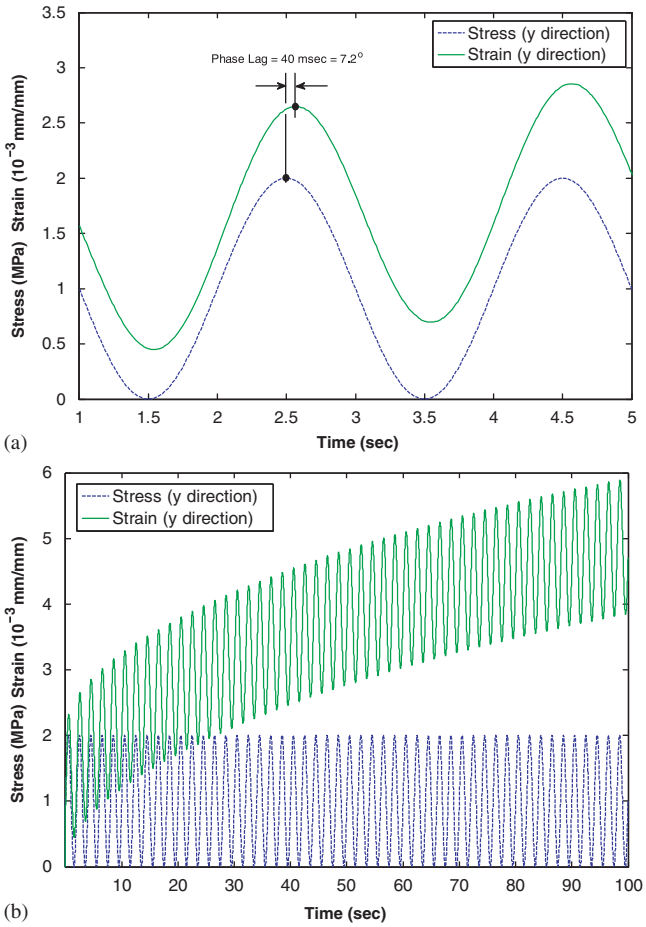


Figure 5. Imposed sinusoidal stress (excitation) and the corresponding strain (response) for viscoelastic body: (a) excitation and response from 1 to 5 s (phase lag of strain is shown) and (b) excitation and response for 100 s.

Table III. Error and computation time analysis for different solution schemes (cyclic loading problem).

| | Direct integration | | | Recursive formulation | | |
|---|---|---|---|---|---|---|
| | Absolute error | | | Absolute error | | |
| Time increment size (s) | Phase lag (deg.) | Strain@100 s ($10^{-6}$ mm/mm) | Solution time (s) | Phase lag (deg.) | Strain@100 s ($10^{-6}$ mm/mm) | Solution time (s) |
| 0.001 | 1.73E−04 | 2.86E−02 | 4.20E+04 | 3.13E−04 | 3.66E−02 | 9.24E+03 |
| 0.002 | 2.37E−04 | 5.94E−02 | 1.90E+04 | 7.31E−04 | 6.14E−02 | 4.72E+03 |
| 0.005 | 7.59E−04 | 1.37E−01 | 5.87E+03 | 1.29E−03 | 1.69E−01 | 2.37E+03 |
| 0.01 | 1.78E−03 | 3.13E+00 | 2.35E+03 | 3.73E−03 | 7.93E+00 | 9.90E+02 |
| 0.02 | 3.83E−03 | 7.63E+00 | 1.26E+03 | 5.92E−03 | 2.76E+01 | 4.31E+02 |
| 0.05 | 8.65E−03 | 1.82E+01 | 7.06E+02 | 1.13E−02 | 6.65E+01 | 2.95E+02 |
| 0.1 | 2.03E−02 | 4.59E+01 | 3.78E+02 | 2.93E−02 | 3.97E+02 | 1.67E+02 |
| 0.2 | 6.59E−02 | 2.01E+02 | 2.16E+02 | 8.20E−02 | 1.47E+03 | 1.07E+02 |

## 5. VERIFICATION

A series of verification examples are simulated to ensure the accuracy of the aforementioned implementation. Preliminary comparisons are made between direct integration and recursive integration



DOI: 10.1002/nag

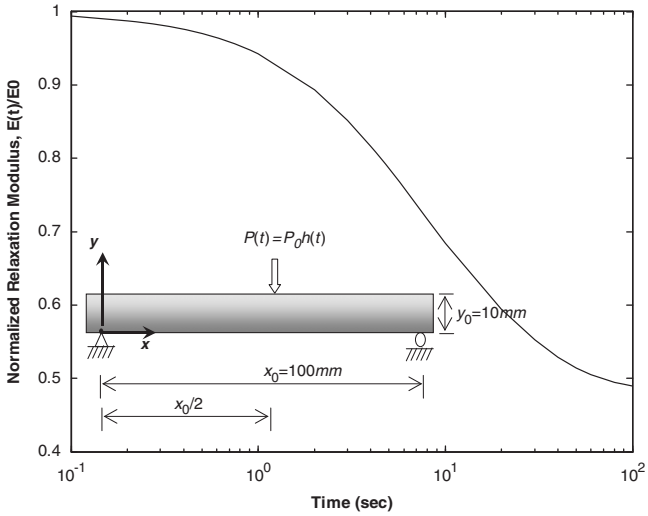


Figure 6. Relaxation modulus for the beam bending verification example (insert: loading and boundary conditions).

schemes. The verifications are made at different levels of sophistication; the initial verification ensures the accuracy of formulation for homogeneous viscoelastic problems. Later examples demonstrate verification for functionally graded viscoelastic boundary value problems. The first set compares VFGM predictions using the present approach with analytical solutions, whereas the second compares the present approach with other numerical simulations.

### 5.1. Three-point bending of viscoelastic beam

A viscoelastic beam in three-point bending is simulated using the recursive FE formulation. The geometry and boundary conditions are shown in Figure 6; the mid-span loading condition is given as

$$P(t) = P_0 h(t), \quad h(t) = \text{Heaviside function} \tag{19}$$

The relaxation modulus for the beam is presented in Figure 6; five Maxwell elements were utilized to represent the relaxation modulus. FE simulations are performed using time-step sizes of 0.1, 1, 2, 5, 10, and 20 s. The normalized mid-span deflections are presented for FE simulations along with analytical solutions in Figure 7. The inset in Figure 7 shows the evolution of error for different time-step sizes. As anticipated, the numerical result converges to the analytical solution as the time-step reduces. The results show that the recursive formulation-based implementation predicts accurate results for the homogeneous viscoelastic boundary value problem when the time-step size is reduced sufficiently.

### 5.2. Relaxation of VFGM bar

This example demonstrates the capability of the recursive FE method to accurately predict the response of a VFGM under step strain loading. The verification example from Mukherjee and Paulino [29] is utilized. The simulations are performed for time-step sizes of 0.1, 0.2, 0.5 and 1 s. The example represents a functionally graded viscoelastic bar undergoing stress relaxation under fixed grip loading. Figure 8 compares numerical results with the exact analytical solution, showing very good agreement.

### 5.3. Creep response of a VFGM bar

This example further verifies the prediction capability of the recursive FE method for VFGM problems. The example involves an exponentially graded viscoelastic bar undergoing creep loading.



DOI: 10.1002/nag

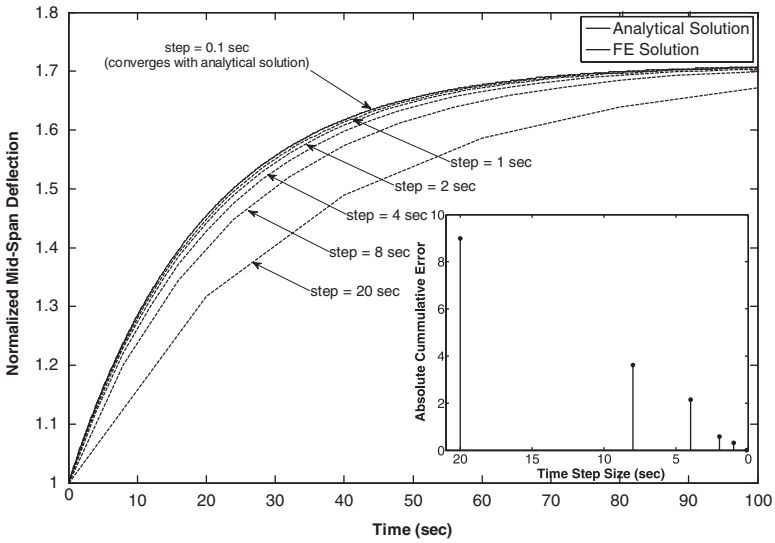


Figure 7. Normalized mid-span deflections for the viscoelastic beam.

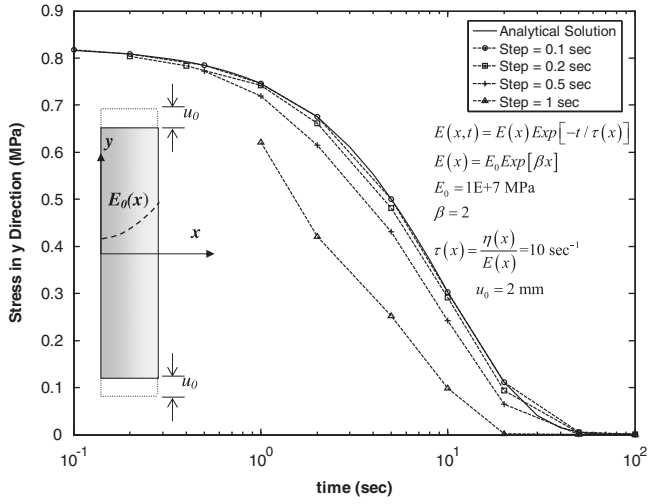


Figure 8. Comparison of exact and numerical solution for the exponentially graded viscoelastic bar in fixed grip loading.

The closed-form solution from Mukherjee and Paulino [29] is compared with the FE predictions. The simulations are performed using a time-step of 0.1 s. Figure 9 compares the numerical results with the analytical solution at different loading times. The results show very good agreement with the analytical solution, further demonstrating the veracity of the viscoelastic-graded FE formulation presented herein and of its successful implementation.

### *5.4. Viscoelastic beam with temperature gradient*

In order to further verify the accuracy of the VFGM FE analysis using the present approach, comparisons are made against the commercial FE software ABAQUS®. The analysis is performed for a viscoelastic beam with a temperature gradient. Temperature-induced property gradients along the thickness ($y$-direction) creates material non-homogeneity. The FGM analysis is compared with layered gradations with varying degree of layer refinements modeled in ABAQUS®. It is important to ensure that the present formulation is capable of capturing temperature-induced



DOI: 10.1002/nag

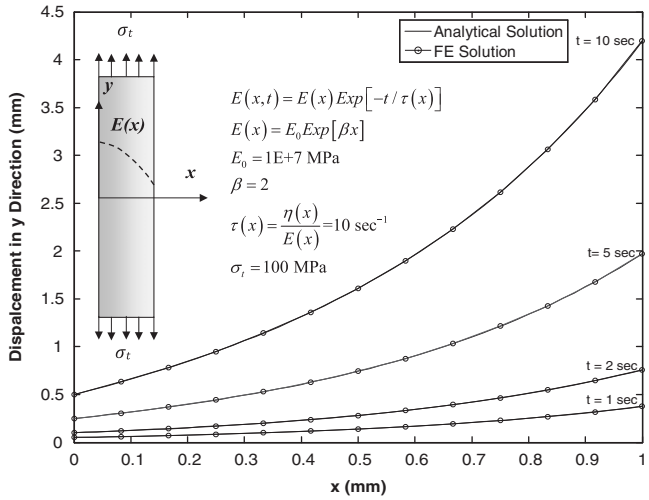


Figure 9. Comparison of exact and numerical solution for the exponentially graded viscoelastic bar in creep loading.

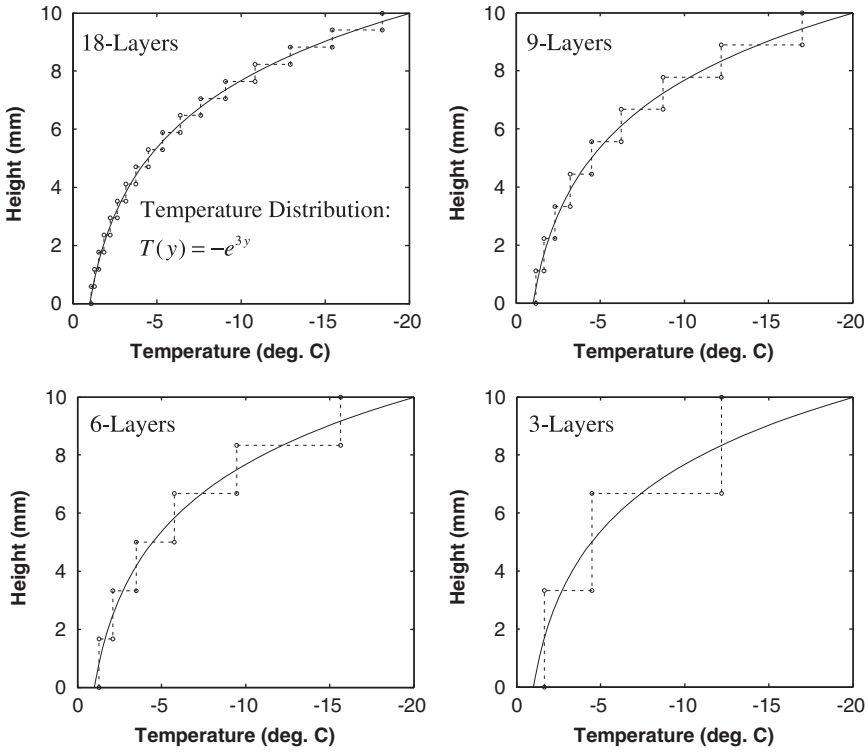


Figure 10. Temperature input for different simulation cases solid line: VFGM approach (present formulation) and dashed line: layered approach (ABAQUS®).

property gradients, as the flexible pavements always exhibit this type of behavior. The loading and geometric conditions for the beam are same as those shown in Figure 6.

The present approach (VFGM) is capable of accurate representation of the temperature distribution, e.g. smoothly graded viscoelastic properties in space and time. In the case of commercial software, the lack of graded elements requires a layered gradation approach. Thus, non-homogeneous properties can be approximated by means of mesh refinement and the assignment of varying properties from layer to layer. For the current problem, the gradation was approximated in ABAQUS



DOI: 10.1002/nag

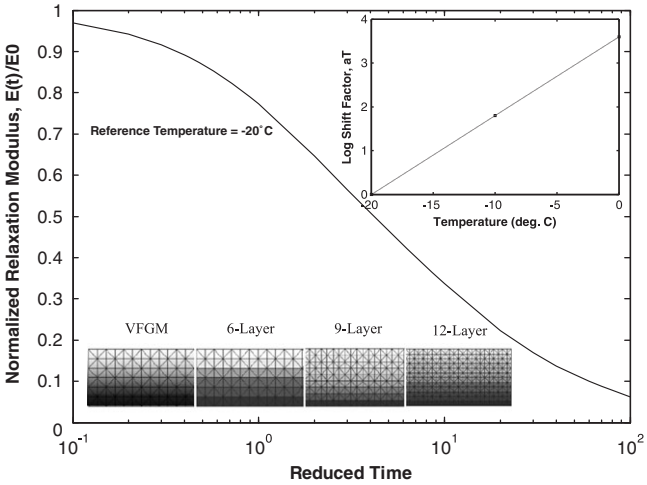


Figure 11. Relaxation modulus and mesh discretization for various simulation cases ($\frac{1}{5}$th beam span shown for each case) (inset: time temperature superposition shift factors).

Table IV. Mesh attributes of different analysis options.

| Simulation case | Number of elements | Number of nodes | Total degrees of freedom |
|---|---|---|---|
| VFGM/6-Layer | 720 | 1573 | 3146 |
| 9-Layer | 1620 | 3439 | 6878 |
| 12-Layer | 2880 | 6025 | 12050 |

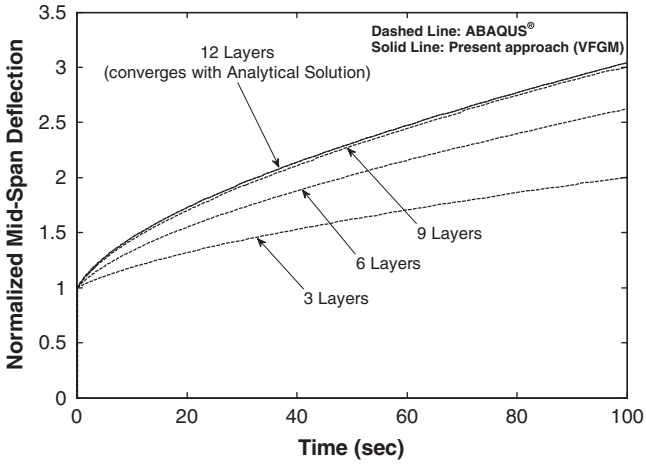


Figure 12. Normalized mid-span deflections for thermally induced graded beam.

using 3, 6, 9, and 18 layers. The temperature distribution for the different simulation cases is presented in Figure 10. The viscoelastic properties for the material are shown in Figure 11. The relaxation modulus mastercurve is plotted at a reference temperature of $-20^{\circ}$C. The inset shows the time–temperature shift factors with the assumption that the material behaves in a thermo-rheologically simple manner. The shift factors link the thermal distribution to the material property distributions as described in Equation (2).

The mesh structures and the mesh statistics for different simulation cases are shown in Figure 11. Note the significant difference between the number of DOF for different simulation cases (c.f. Table IV). The simulation results are plotted in Figure 12. The results for the problem



DOI: 10.1002/nag

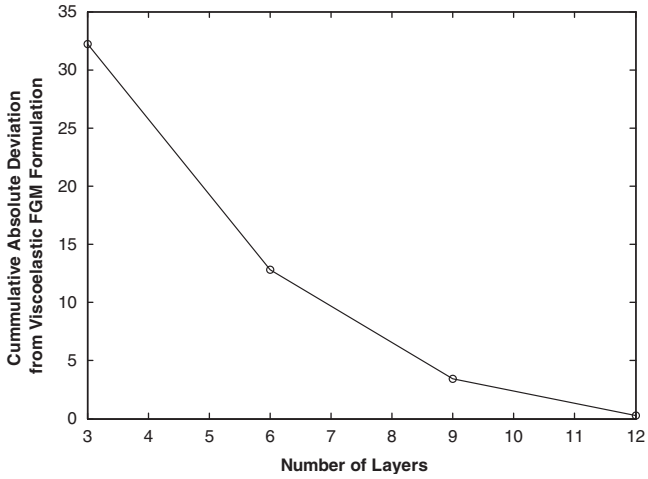


Figure 13. Deviation of layered results with VFGM results.

are presented in the form of normalized mid-span deflections as function of time. The results demonstrate the accuracy of the present formulation in capturing temperature-induced viscoelastic property gradients. With the increasing mesh refinement, the layered approach begins to converge with the FGM results. Figure 13 shows the deviation of the layered approach from the VFGM approach. This plot illustrates the greater efficiency of the present approach as compared to the traditional layered approach.

## 6. VFGM BOUNDARY LAYER ANALYSIS

A large variety of flexible pavement distresses are caused due to initiation and propagation of cracks in pavements, including thermal cracking, fatigue cracking, top–down cracking and reflective cracking. As a result of aging and non-uniform temperature distribution, pavements exhibit functionally graded viscoelastic behavior. In order to predict cracking in flexible pavements, it is important to accurately determine the crack-tip stress fields. This section describes crack-tip stress fields in radially graded viscoelastic material, determined using a boundary layer model.

Williams [39] presented the stationary crack-tip stress and displacement fields, and Eischen [40] extended them for elastic non-homogeneous bodies with continuous, differentiable, and bounded material properties. The stress fields and corresponding displacements as derived by Eischen are as follows:

$$\begin{aligned} \sigma_{ij} &= \frac{K_{\mathrm{I}}}{\sqrt{2\pi r}} f_{ij}^{\mathrm{I}}(\theta) + \frac{K_{\mathrm{II}}}{\sqrt{2\pi r}} f_{ij}^{\mathrm{II}}(\theta) + T\delta_{i1}\delta_{j1} + O(r^{1/2}) \\ u_i &= \frac{K_{\mathrm{I}}}{G_{\mathrm{tip}}}\sqrt{\frac{r}{2\pi}} g_i^{\mathrm{I}}(\theta) + \frac{K_{\mathrm{II}}}{G_{\mathrm{tip}}}\sqrt{\frac{r}{2\pi}} g_i^{\mathrm{II}}(\theta) + O(r) \end{aligned} \tag{20}$$

where $K_{\mathrm{I}}$ and $K_{\mathrm{II}}$ are mode I and mode II stress intensity factors (SIFs), respectively, $f_{ij}(\theta)$ and $g_i(\theta)$ are angular functions for stresses and displacements, respectively, and $T$ is the $T$-stress.

Marur and Tippur [41] utilized FEM for investigation of crack-tip stress fields in FGMs. Kim [42] investigated crack-tip stresses in exponentially graded materials through use of a boundary layer model and evaluated auxiliary fields for FGMs. Paulino and Zin [12, 13] have proposed analytical solutions for crack-tip stresses in VFGMs using the correspondence principle. Owing to limitations of the correspondence principle, the previous solutions are limited to materials with spatial dependence on only time-independent quantities. Recently, Pan *et al.* [43] have studied multiple cracks in VFGMs; however, they have utilized conventional homogeneous FEs available



DOI: 10.1002/nag

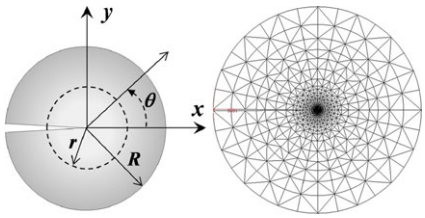


Figure 14. Problem description and FE model.

in commercial software for the prediction of crack-tip stresses using layered gradations. In the current study, the material non-homogeneity is captured with greater accuracy and efficiency than the layered approaches through the use of the GIF. The use of time-integration schemes allows for a material model that has spatial dependence on both elastic and viscous properties, making it more general than the previous studies.

### 6.1. Problem description and FE mesh

Figure 14 shows the problem description along with the angular convention. Among others, Eftis *et al.* [44] have presented the loading conditions on the outer boundary corresponding to the asymptotic stresses at the crack tip. In the current example, Mode I displacement loading conditions were assumed. These are given by

$$\begin{aligned} u_i &= \frac{K_{\mathrm{I}}}{G_{\mathrm{tip}}}\sqrt{\frac{r}{2\pi}}g_i^{\mathrm{I}}(\theta) \quad \text{where } g_1^{\mathrm{I}}(\theta)=\cos\frac{\theta}{2}\left[\frac{1}{2}(\kappa-1)+\sin^2\frac{\theta}{2}\right] \quad \text{and} \\ g_2^{\mathrm{I}}(\theta) &= \sin\frac{\theta}{2}\left[\frac{1}{2}(\kappa+1)-\cos^2\frac{\theta}{2}\right] \end{aligned} \tag{21}$$

The FE model was developed with 3232 elements and 6599 nodes using six node plane stress triangular elements (T6). Figure 14 shows the FE mesh; the average element side length of $0.2\times R$ was utilized along the periphery which was reduced to $10^{-4}\times R$ at the center.

### 6.2. Material gradation

Elastic and viscoelastic simulations were performed for a VFGM with radial gradations. A generalized Maxwell model is utilized for the representation of a time- and space-dependent material. The functional form of the material properties and the gradation for various components of the generalized Maxwell model are shown in Equation (22). Notice that the stiffness of the material at any given time is greatest along the periphery and lowest at the center of the body. The material gradation is illustrated in Figure 15, which shows the variation of relaxation modulus with time and radial distance, $r$. In addition to the VFGM material, two cases representing the most compliant and stiff material properties are simulated; these are recovered from Equation (22) for $r=0$ (compliant) and $r=R$ (stiff).

$$\begin{aligned} E(r,t) &= \sum_{i=1}^{2} E_i(r)\,\mathrm{Exp}\left(-\frac{t}{\tau_i(r)}\right) \\ E_i(r) &= E_0\,\mathrm{Exp}\left(a\frac{r}{R}\right), \quad \tau_1(r)=b\left(1+\frac{r}{R}\right)^c, \quad \tau_2(r)=d\left(1-\mathrm{Exp}\left(e\frac{r}{R}\right)\right) \end{aligned} \tag{22}$$

$a$, $b$, $c$, $d$, and $e$ are all scalar material constants.

### 6.3. Results

The elastic stress fields for the homogeneous cases are first visited to ensure the accuracy of the FE solutions. The results at instantaneous loading (time, $t=0$) for the 'stiff' material are shown in Figure 16. The plot shows the variation of stresses as a function of the angle, $\theta$. The results



DOI: 10.1002/nag

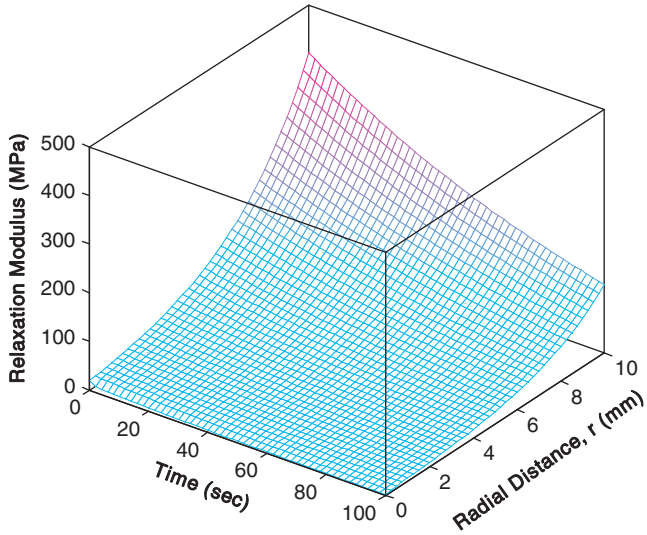


Figure 15. Relaxation modulus variation with radial distance and time.

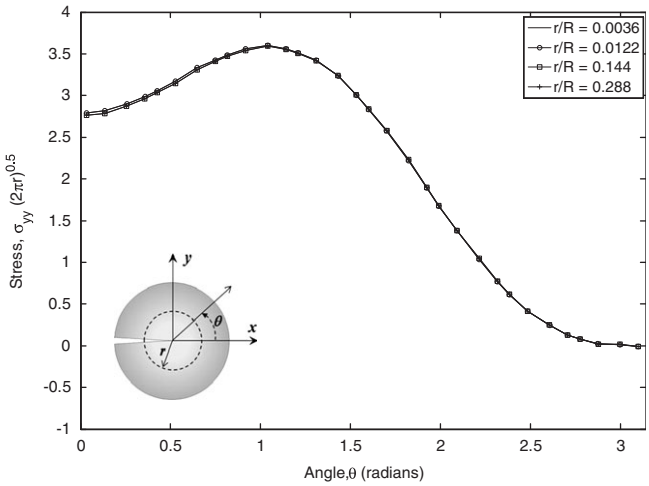


Figure 16. Elastic stresses for homogeneous 'stiff' properties at different radial distances.

are shown for four radial distances and, as anticipated, the predicted stresses match closely with the reference solution. This set of results provides confidence that the displacement boundary conditions are accurately imposed and the elastic FE analysis yields correct results.

The elastic normal and shear stress fields for both homogeneous material distributions and FGM distribution are presented in Figure 17. Stresses for FGM are shown for one radial distance ($r/R = 0.012$). The elastic stresses match the results reported by previous researchers, for instance, Kim [42]. The FGM stress fields are consistently in between the 'stiff' and 'compliant' materials, as expected. Notice that as the deflection angle approaches the crack ($\theta = \pi$), the stress-free conditions are recovered. In order to demonstrate the effect of radial gradation on elastic stresses, normal stresses are plotted at different radial distances for the FGM along with homogeneous materials (c.f. Figure 18).

The normal stresses ($y$-direction) for simulations conducted with homogeneous and VFGM assumptions are shown in Figure 19. The results clearly exhibit viscoelastic stress relaxation with increasing time. In order to further explore the stress relaxation tendencies, the peak normal stresses for each material type are plotted against time, as shown in Figure 20. It should be noted that the



DOI: 10.1002/nag

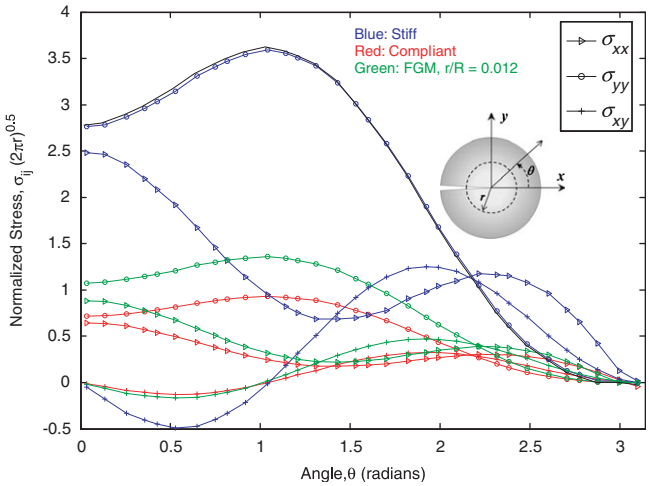


Figure 17. Elastic stresses for all material distributions (homogeneous and FGM).

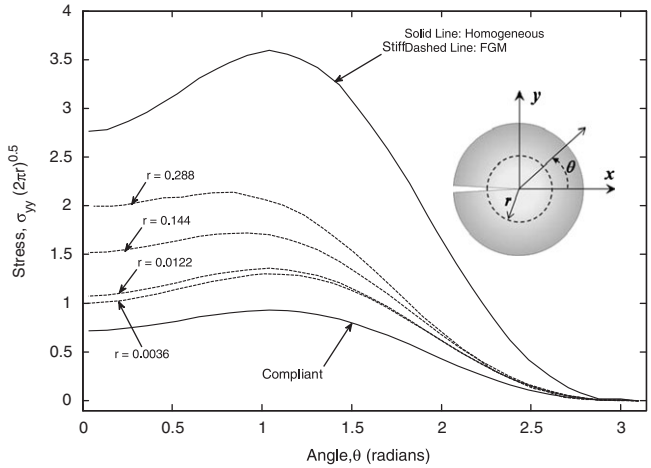


Figure 18. Elastic stresses ($y$-direction) for FGM (at four radial distances) and homogeneous materials.

relaxation of stresses is not distributed evenly with time. This trend illustrates the graded nature of the time-dependent material properties. If the spatial gradation of constitutive model parameters was limited to elastic components, the plots would have shown constant deviation between different radial distances. For this example, the time effect of property gradation is most pronounced between the radial distances of $r/R = 0.0122$ and $r/R = 0036$. The shear stresses for all material types are shown in Figure 21. The greatest shear stresses are observed at shortest loading times and for the stiffest material properties. Stress relaxation is evident in all cases as with the normal stresses. Figure 22 shows the peak shear stresses for both homogeneous material distributions and at four radial distances for VFGM. The relaxation behavior of stresses again demonstrates the effect of combined spatial and temporal variations in properties.

### *6.4. Summary of boundary layer analysis*

A radially graded viscoelastic FGM in mode-I loading conditions was simulated to study the crack-tip responses. The elastic stress fields match the results presented by previous researchers, further verifying the accuracy and efficiency of the GIF elements developed in this study. The viscoelastic crack-tip stresses are shown for loading times up to 100 s. The effect of non-homogeneous, time-dependent constitutive properties are evident in the observed responses.



DOI: 10.1002/nag

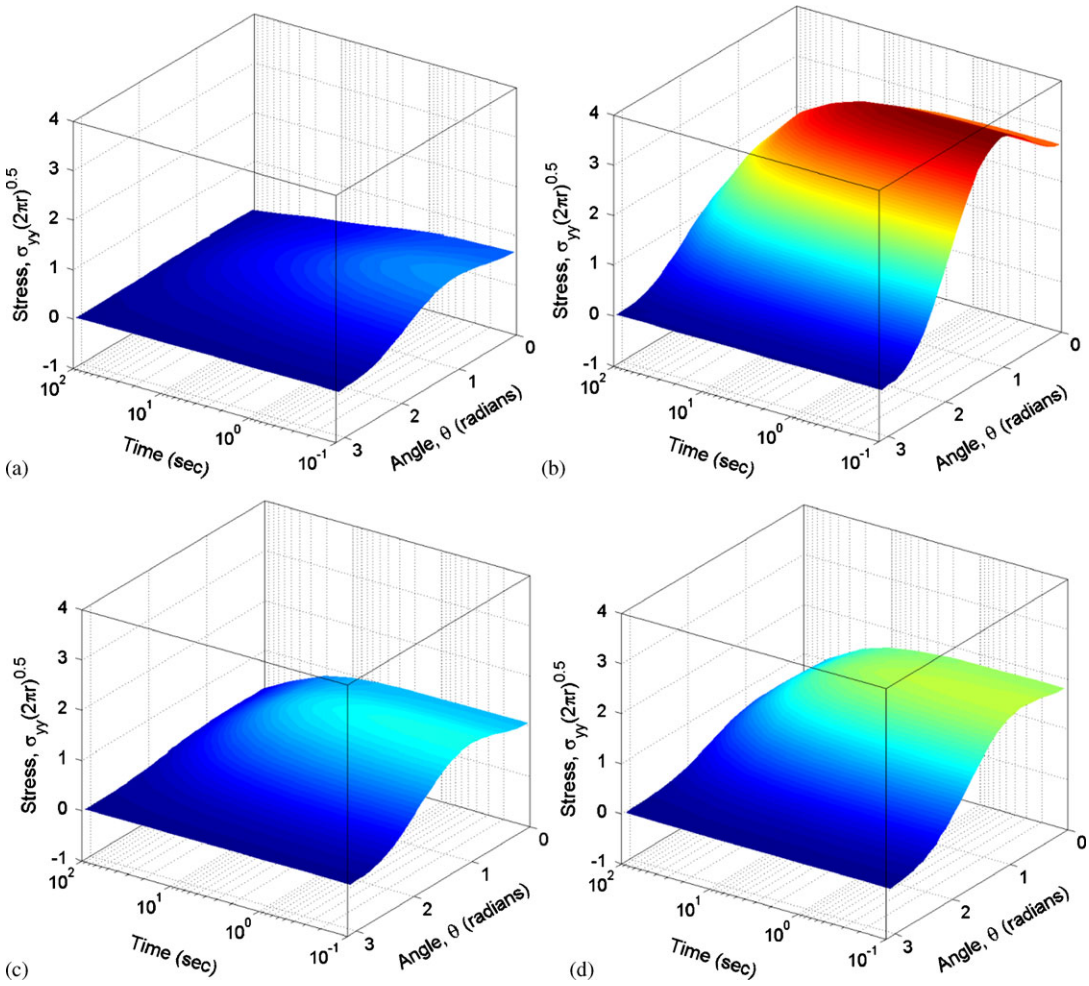


Figure 19. Viscoelastic normal stresses ($y$-direction) for all material distributions (homogeneous and VFGM): (i) homogeneous material—(a) compliant material and (b) stiff material, and (ii) VFGM—(a) $r/R = 0.0122$ and (b) $r/R = 0.288$.

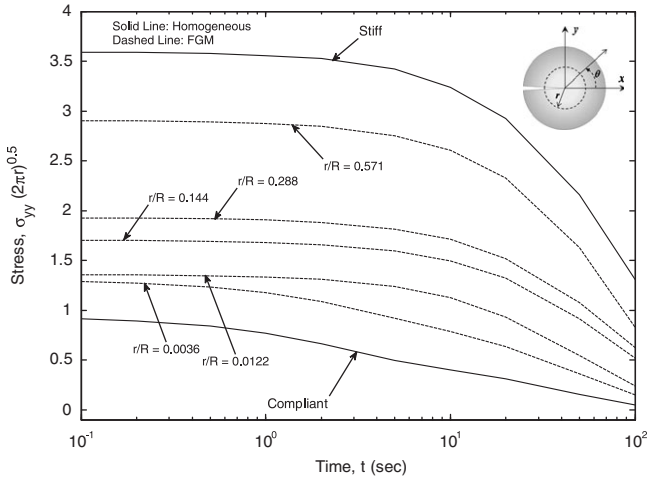


Figure 20. Peak normal stresses ($y$-direction) for all material distributions (homogeneous and VFGM).



DOI: 10.1002/nag

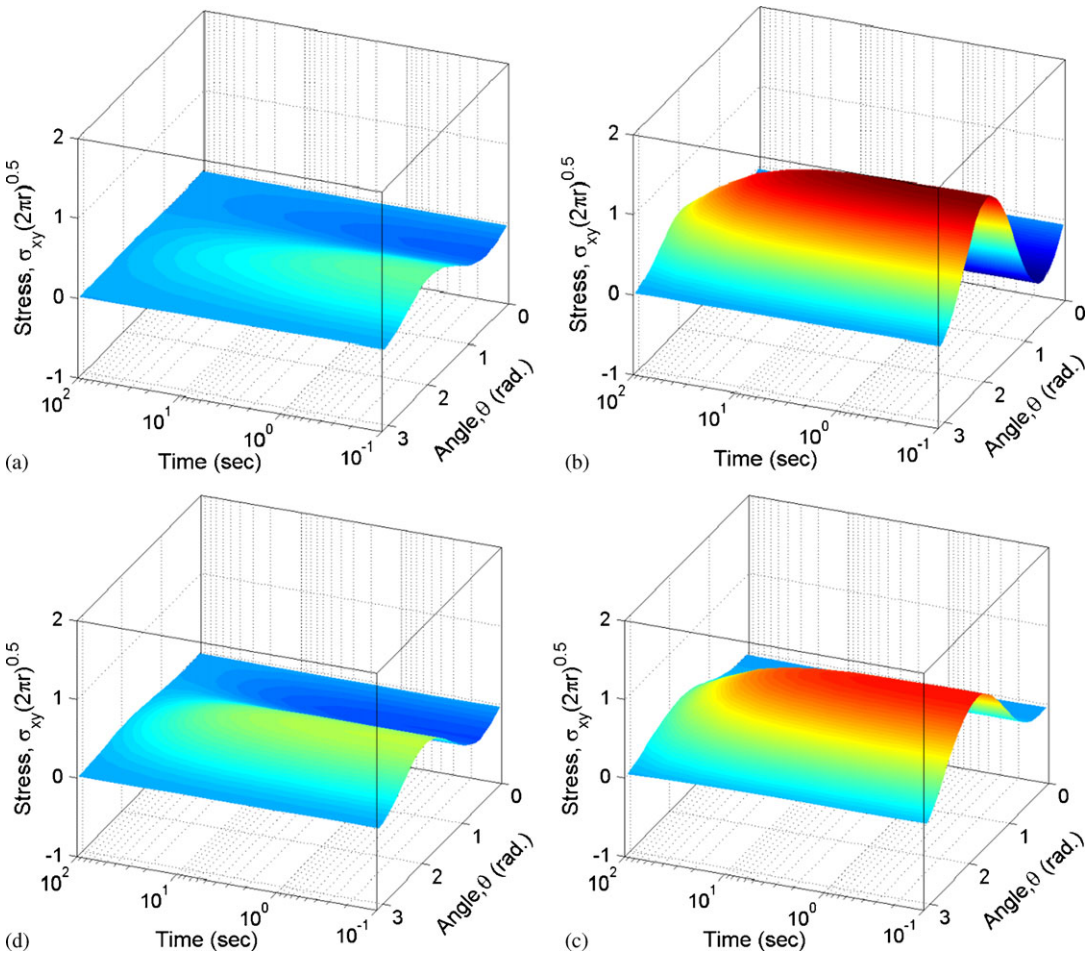


Figure 21. Viscoelastic shear stresses for all material distributions (homogeneous and VFGM): (i) homogeneous material—(a) compliant material and (b) stiff material, and (ii) VFGM—(a) $r/R = 0.0122$ and (b) $r/R = 0.288$.

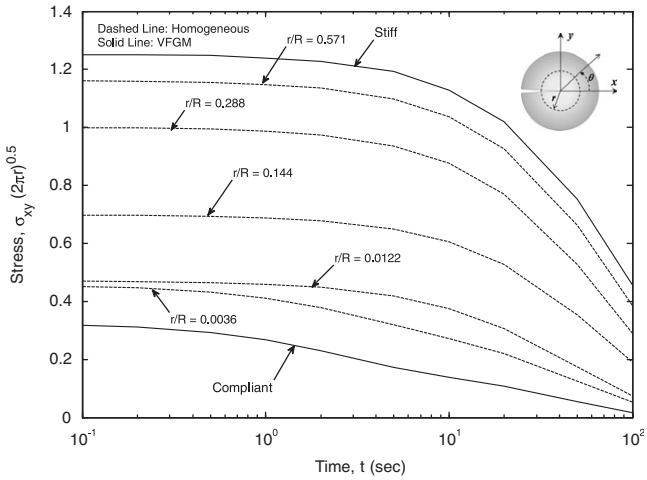


Figure 22. Peak shear stresses for all material distributions (homogeneous and VFGM).



DOI: 10.1002/nag

## 7. ASPHALT PAVEMENT WITH GRADED INTERFACE

### *7.1. Introduction and motivation*

The current state of practice in modeling of asphalt concrete pavements is to assign infinitesimally small thickness to the interface between different asphalt courses or lifts [45–48]. In the current example, this type of approach is labeled as 'Stepped Interface' due to the sudden jump in material properties at the boundary. The viscoelastic FGM FE analysis procedure developed in this paper is a useful tool for the simulation of viscoelastic interfaces. This example compares the responses obtained for graded versus stepped interfaces in the context of asphalt pavement analysis.

### *7.2. Pavement section*

A pavement section from Louisiana State Highway, LA34 located near the town of Monroe in northern Louisiana is selected as the basis for constructing the simulation model. The pavement section was constructed in the form of an overlay-interlayer system. This pavement is a part of the National Science Foundation (NSF) sponsored reflective cracking study by Paulino *et al.* [49]. Figure 23 shows the selected pavement section, which undergoes heavy truck traffic due to its close proximity to a paper mill.

### *7.3. FE model and boundary conditions*

The FE model for the pavement analysis is developed on the basis of the pavement information obtained from site visits as well as the cross-section details obtained from construction plans and cored samples. Figure 24 shows the cross-section of the pavement as utilized for the FE

Figure 23. Pavement section (LA34 near Monroe, LA).

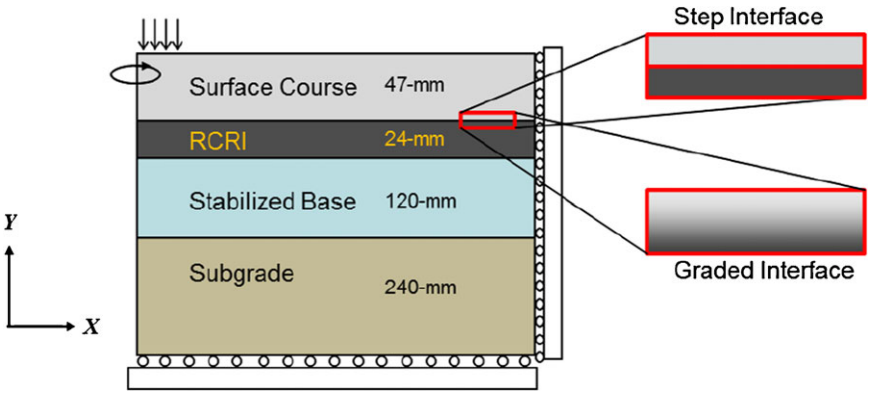


Figure 24. Pavement cross-section and FE model schematics.



DOI: 10.1002/nag

model construction. The FE simulations are performed using an assumption of 2D axisymmetric conditions.

As described previously, the focus of this example is to compare two simulation approaches for interfaces between asphalt concrete construction lifts; Figure 24 illustrates the two simulation approaches regarding the representation of interface between asphalt concrete lifts, namely, step interface and graded interface.

Two key properties are needed for accurate simulation of graded interfaces, (1) height or width of interface, and (2) distribution of material properties within the interface. In this example, the following assumptions are made:

- The width of interface is 9.5 mm; this assumption is made on the basis of the nominal maximum aggregate sizes (NMAS) of the asphalt mixtures. The surface course is a 19 mm NMAS mixture and the reflective crack relief interlayer (RCRI) mixture is 4.75 mm NMAS.
- The material properties are assumed to be transitioning in a linear fashion from one mixture to another over the thickness of the interface. A better approach for obtaining viscoelastic property gradation at the interfaces would be to incorporate micromechanical approaches such as those proposed by Yin *et al.* [50]. This has been identified as one of the future extensions of this work.

### *7.4. AC material properties*

Wagoner *et al.* [51] have tested and analyzed field core samples from the LA34 highway. The relaxation moduli for overlay and interlayer mixtures are shown in Figure 25. The variation of material properties at the interface for 'step interface' and 'graded interface' are shown in Figures 26 and 27, respectively. The granular base and soil subgrade are modeled as elastic materials with Young's modulus of 276 and 158 MPa, and Poisson's ratio of 0.2 and 0.45, respectively. Note the mismatch of properties at the midpoint of the interface for the stepped approach.

### *7.5. Results*

The response parameter that is utilized for comparing the two simulation approaches is the stress in the horizontal direction directly under the tire load. Figure 28 shows the variation of stresses as a function of vertical position in the asphalt layer. The results are presented for 10, 100, and 100 s loading times. Note that the stresses exhibit an unrealistic 'jump' at the interface. This jump in stresses is illustrated in Figure 29; the plot shows variation of as much as 49% between the predicted tensile stresses at the bottom of the overlay. The tensile stresses at the bottom of the overlay are important for simulations of reflective cracking. In particular, the tensile stresses

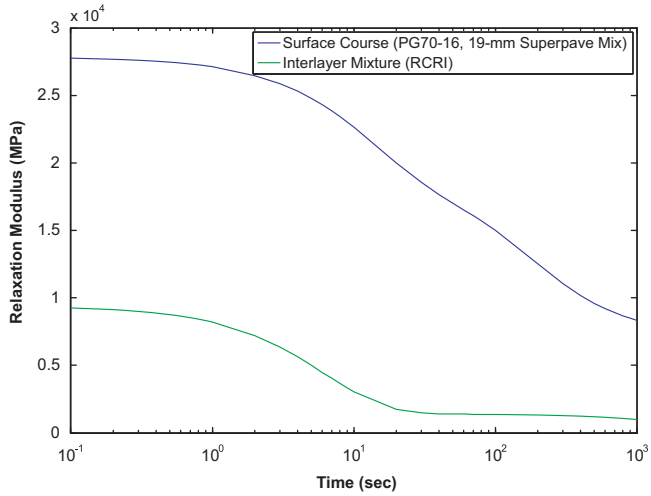


Figure 25. Relaxation modulus for surface and interlayer mixtures.



DOI: 10.1002/nag

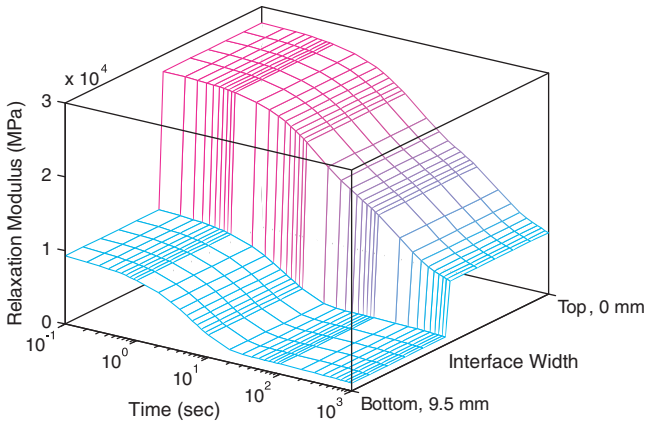


Figure 26. Relaxation modulus variation for step interface.

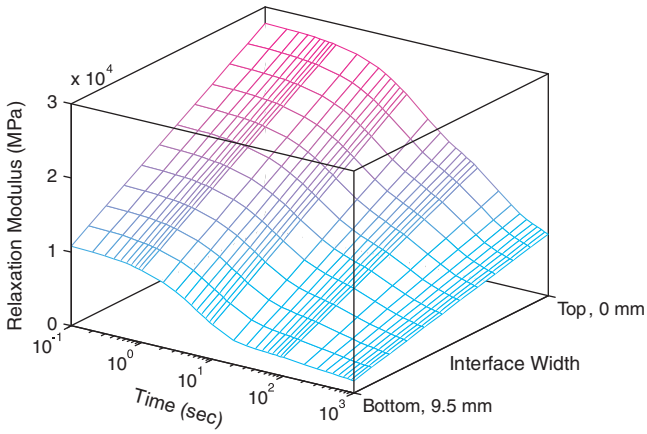


Figure 27. Relaxation modulus variation for graded interface.

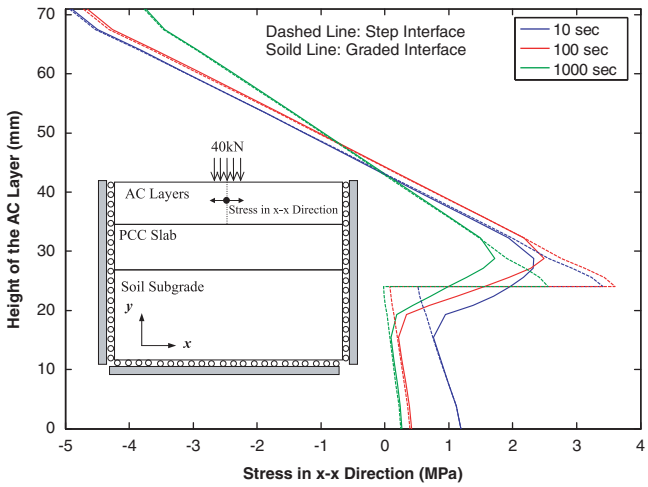


Figure 28. Stress in horizontal direction ($x$-direction) directly under the tire load (different loading times are shown).



DOI: 10.1002/nag

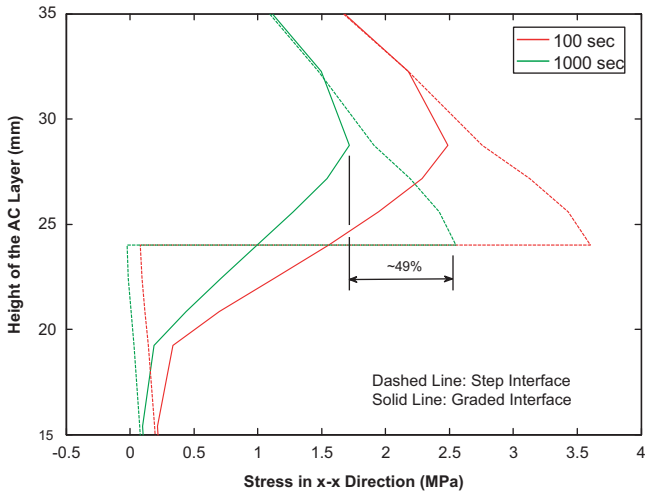


Figure 29. Stress in horizontal direction ($x$-direction) at interface.

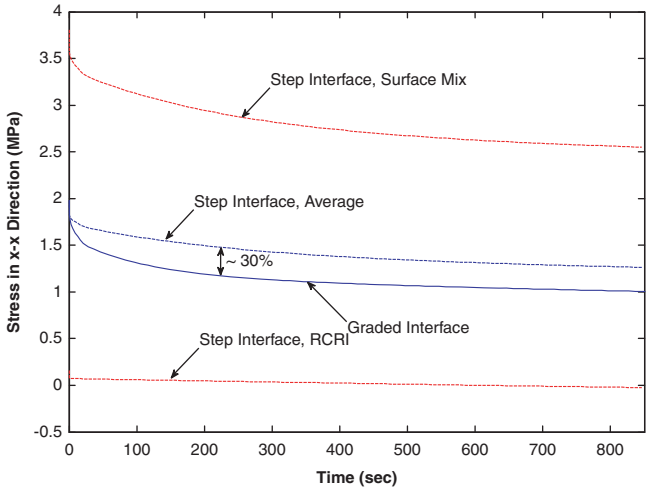


Figure 30. Peak tensile stresses in the overlay.

are compared with the tensile strength of the material, which serves as the threshold parameter for the onset of damage. While for this particular example, the step interface approach yields additional factor of safety in the design, for other pavement distresses, such as top–down cracking and low-temperature cracking, the step interface would not yield a conservative response.

The variations of peak tensile stresses within the interface as a function of loading time are shown in Figure 30. The plot shows peak stresses for the graded interface and three sets of plots for step interfaces: (1) peak stress for the surface course, (2) peak stress for RCRI, and (3) average of surface course and RCRI stresses. The motivation for plotting average stresses for the step interface is to demonstrate that simple averaging of responses (stresses or strains) at the interface significantly over predicts the response compared with the graded interface. For the current example, the averaging approach yields as much as 30% over prediction as compared with the graded interface approach.

### *7.6. Summary and findings*

An example is presented for an overlay–interlayer pavement system based on an actual pavement section on Louisiana state highway 34. The interface between the overlay and interlayer is modeled



DOI: 10.1002/nag

using two approaches, a more conventional step interface and a more physically graded interface. The graded interface is assumed to have a thickness of 9.5 mm and the viscoelastic properties are assumed to be varying linearly within the interface. Based upon this limited study, the following key points are observed:

- The physical interfaces between different asphalt lifts require special modeling considerations.
- The assumption of an interface with infinitesimal thickness (step interface) yields unrealistic stress responses for material layers, which are known to have interpenetration in practice.
- The limited study shown here demonstrated significant variation between peak tensile stresses obtained from step and graded interfaces.
- The average stresses computed for step interfaces were also found to be significantly greater than those obtained from graded interface modeling.

## 8. CONCLUSIONS AND EXTENSIONS

In order to achieve accurate response predictions, it is important to consider non-homogeneities in flexible pavements and geotechnical structures. Viscoelastic functionally graded FEs using GIFs are proposed together with a recursive time-integration formulation. The procedures developed herein are suitable and preferred for functionally graded viscoelastic problems, such as flexible pavements with aging and temperature-dependent property gradients. A series of verifications are performed to demonstrate the veracity of the formulation and its implementation.

Two application examples are discussed demonstrating the applicability of the current approach for investigation of cracking in VFGMs and for response prediction of asphalt concrete pavements with graded interfaces. These examples further illustrate the suitability of the present approach for the analysis of flexible pavements.

Further extensions of the current work include exploration of the length scales and property distributions of the interfaces between asphalt concrete layers. Other extensions include application of the current work to other graded viscoelastic systems such as geotechnical structures, polymeric composites, and fiber-reinforced cement concrete.

ACKNOWLEDGEMENTS

The authors would like to acknowledge the support from the United States Department of Transportation's (USDOT) NexTrans Research Center and the Federal Highway Administration (FHWA) Pooled Fund Study TPF-5(132). Any opinions expressed herein are those of the writers and do not necessarily reflect the views of the sponsors. They also thank Ms Sofie E. Léon for her help in the preparation of this manuscript.

REFERENCES

1. Federal Highway Administration. Miles by type of surface and ownership, functional system national summary. Federal Highway Administration, HM-12, Washington, D.C., 2008.
2. NCHRP Project. Guide for mechanistic–empirical design of new and rehabilitated pavement structures. *NCHRP Project 1-37A Final Report*, ARA Inc., ERES Consultants, 2002.
3. Suresh S, Mortensen A. Functionally graded materials. *The Institute of Materials*. IOM Communications Ltd.: London, 1998.
4. Cavalcante MAA, Marques SPC, Pindera M. Parametric formulation of the finite-volume theory for functionally graded materials—part I: analysis. *Journal of Applied Mechanics* 2007; **74**:935–945.
5. Miyamoto Y, Kaysser WA, Rabin BH (eds). *Functionally Graded Materials*: *Design, Processing and Applications*. Kluwer: Dordrecht, The Netherlands, 1999.
6. Bang DPV, Di Benedetto H, Duttine A, Ezaoui A. Viscous behaviour of dry sand. *International Journal for Numerical and Analytical Methods in Geomechanics* 2007; **31**:1631–1658.
7. Sanchez-Giron V, Andreu E, Hernanz JL. Stress relaxation of five different soil samples when uniaxially compacted at different water contents. *Soil and Tillage Research* 2001; **62**:85–99.
8. Wei C, Muraleetharan KK. Linear viscoelastic behavior of porous media with non-uniform saturation. *International Journal of Engineering Science* 2007; **45**:698–715.



DOI: 10.1002/nag

9. Vinogradov AM. Generalized approach to the structure–soil interaction analysis with time and temperature effects. *POAC 85*: *The Eighth International Conference on Port and Ocean Engineering under Actic Conditions*, Narssarssuaq, Greenland, vol. 1, 1985; 468–477.
10. Dong Guo W. Visco-elastic consolidation subsequent to pile installation. *Computers and Geotechnics* 2000; **26**:113–144.
11. Roesler JR, Paulino GH, Gaedicke C, Bordelon A, Park K. Fracture behavior of functionally graded concrete materials for rigid pavements. *Transportation Research Record* 2007; **2037**:40–49.
12. Paulino GH, Jin ZH. Viscoelastic functionally graded materials subjected to antiplane shear fracture. *Journal of Applied Mechanics* 2001; **68**:284–293.
13. Jin ZH, Paulino GH. A viscoelastic functionally graded strip containing a crack subjected to in-plane loading. *Engineering Fracture Mechanics* 2002; **69**:1769–1790.
14. Altenbach H, Eremeyev VA. On the bending of viscoelastic plates made of polymer foams. *Acta Mechanica* 2009; **204**:137–154.
15. AASHTO. Standard test method for determining the creep compliance and strength of hot mix asphalt (HMA) using the indirect tensile test device (T-322). American Association of State Highway and Transportation Officials, Washington, D.C., 2004.
16. Santare MH, Lambros J. Use of graded finite elements to model the behavior of nonhomogeneous materials. *Journal of Applied Mechanics* 2000; **67**:819–822.
17. Kim JH, Paulino GH. Isoparametric graded finite elements for nonhomogeneous isotropic and orthotropic materials. *Journal of Applied Mechanics* 2002; **69**:502–514.
18. Zhang Z, Paulino GH. Wave propagation and dynamic analysis of smoothly graded heterogeneous continua using graded finite elements. *International Journal of Solids and Structures* 2007; **44**:3601–3626.
19. Silva ECN, Carbonari RC, Paulino GH. On graded elements for multiphysics applications. *Smart Materials and Structures* 2007; **16**:2408–2428.
20. Hilton HH, Yi S. Anisotropic viscoelastic finite element analysis of mechanically and hygrothermally loaded composites. *Composites Engineering* 1993; **3**:123–135.
21. Muliana A, Khan KA. A time-integration algorithm for thermo-rheologically complex polymers. *Computational Materials Science* 2008; **41**:576.
22. Zienkiewicz OC, Watson M, King IP. A numerical method of visco-elastic stress analysis. *International Journal of Mechanical Sciences* 1968; **10**:807–827.
23. Taylor RL, Pister KS, Goudreau GL. Thermomechanical analysis of viscoelastic solids. *International Journal for Numerical Methods in Engineering* 1970; **2**:45–59.
24. Zocher MA, Groves SE, Allen DH. A three-dimensional finite element formulation for thermoviscoelastic orthotropic media. *International Journal for Numerical Methods in Engineering* 1997; **40**:2267–2288.
25. Yi S, Hilton HH. Dynamic finite element analysis of viscoelastic composite plates in the time domain. *International Journal for Numerical Methods in Engineering* 1994; **37**:4081–4096.
26. Sladek J, Sladek V, Zhang C, Schanz M. Meshless local Petrov–Galerkin method for continuously nonhomogeneous linear viscoelastic solids. *Computational Mechanics* 2006; **37**:279–289.
27. Gilhooley DF, Xiao JR, Batra RC, McCarthy MA, Gillespie JWJ. Two-dimensional stress analysis of functionally graded solids using the MLPG method with radial basis functions. *Computational Materials Science* 2008; **41**:467–481.
28. Dave EV, Paulino GH, Buttlar WG. Viscoelastic functionally graded finite element method using correspondence principle. *Journal of Materials in Civil Engineering* (ASCE) 2011; **23**:39–48.
29. Mukherjee S, Paulino GH. The elastic-viscoelastic correspondence principle for functionally graded materials, revisited. *Journal of Applied Mechanics* 2003; **70**:359–363.
30. Rajagopal KR, Wineman AS. A quasi-correspondence principle for Quasi-Linear viscoelastic solids. *Mechanics of Time-dependent Materials* 2008; **12**:1–14.
31. Hilton HH. Viscoelastic analysis. *Engineering Design for Plastics*. Reinhold: New York, 1964; 1–199.
32. Christensen RM. *Theory of Viscoelasticity*. Dover: Mineola, New York, 1982.
33. Cook RD, Malkus DS, Plesha ME. *Concepts and Applications of Finite Element Analysis* (4th edn). Wiley: New York, 2001.
34. Reddy JN. *An Introduction to Finite Element Method* (3rd edn). McGraw-Hill: New York, 2005.
35. Gurtin ME. Variational principles in the linear theory of viscoelasticity. *Archives of Rational Mechanics and Analysis* 1963; **36**:179–185.
36. Song SH. Fracture of asphalt concrete: a cohesive zone modeling approach considering viscoelastic effects. *Doctorate Thesis*, University of Illinois at Urbana-Champaign, Urbana, IL, 2006.
37. Song SH, Paulino GH, Buttlar WG. A bilinear cohesive zone model tailored for fracture of asphalt concrete considering viscoelastic bulk material. *Engineering Fracture Mechanics* 2006; **73**:2829–2848.
38. Wagoner MP, Buttlar WG, Paulino GH. Disk-shaped compact tension test for asphalt concrete fracture. *Proceedings of the Society for Experimental Mechanics*, *Inc* 2005; **52**:270–277.
39. Williams ML. On stress distribution at base of stationary crack. *Journal of Applied Mechanics* 1957; **24**:109–114.
40. Eischen JW. Fracture of nonhomogeneous materials. *International Journal of Fracture* 1987; **34**:3–22.
41. Marur PR, Tippur HV. Numerical analysis of crack-tip fields in functionally graded materials with a crack normal to the elastic gradient. *International Journal of Solids and Structures* 2000; **37**:5353–5370.




DOI: 10.1002/nag

42. Kim JH. Mixed-mode crack propagation in functionally graded materials. *Doctorate Thesis*, University of Illinois at Urbana-Champaign, Urbana, IL, 2003.
43. Pan F, Li W, Wang B, Zhang X. Viscoelastic fracture of multiple cracks in functionally graded materials. *Computer Methods in Applied Mechanics and Engineering* 2009; **198**:2643–2649. DOI: 10.1016/j.cma.2009.03.005.
44. Eftis J, Subramonian N, Liebowitz H. Biaxial load effects on the crack border elastic strain energy and strain energy rate. *Engineering Fracture Mechanics* 1977; **9**:753–764.
45. Dave EV, Braham AF, Buttlar WG, Paulino GH, Zofka A. Integration of laboratory testing, field performance data, and numerical simulations for the study of low-temperature cracking. *Proceedings of the Sixth RILEM International Conference on Cracking in Pavements*, vol. 1, 2008; 369–378.
46. Khazanovich L, Wang Q. MnLayer: high-performance layered elastic analysis program. *Transportation Research Record* 2007; **2037**:63–75.
47. Baek J, Al-Qadi IL. Finite element method modeling of reflective cracking initiation and propagation: investigation of the effect of steel reinforcement interlayer on retarding reflective cracking in hot-mix asphalt overlay. *Transportation Research Record* 2006; **1949**:32–42.
48. Novak M, Birgisson B, Roque R. Tire contact stresses and their effects on instability rutting of asphalt mixture pavements: three-dimensional finite element analysis. *Transportation Research Record* 2003; **1853**:150–156.
49. Paulino GH, Buttlar WG, Blankenship PB, Dave EV, Wagoner MP, Song SH. Reflective crack control treatment and design procedures: a new integrated approach. *CMS 0219566*, National Science Foundation, Washington, D.C., 2007.
50. Yin HM, Paulino GH, Buttlar WG, Sun LZ. Micromechanics-based thermoelastic model for functionally graded particulate materials with particle interactions. *Journal of the Mechanics and Physics of Solids* 2007; **55**:132–160.
51. Wagoner MP, Buttlar WG, Paulino GH, Blankenship PB. Laboratory testing suite for characterization of asphalt concrete mixtures obtained from field cores. *Journal of Asphalt Paving Technologists*, *Proceedings of the Annual Meeting*, *Association of Asphalt Paving Technologists* 2006; **75**:815–852.



DOI: 10.1002/nag